OE Optical Engineering

RESEARCH PAPER

Single-cell high-precision ablation using nanosecond-pulsed thulium-doped fiber laser

Matthew D. Gerard,[a,†] Hiroki Cook,[b,c,†] James A. Read,[b,c] Ibrahim H. Abughazaleh,[a] Panuwat Srisamran,[a] Siddhi Chugh,[b,c] Sijing Liang,[a] Qiang Fu,[a] Richard O. C. Oreffo,[d] David J. Richardson,[a] Sumeet Mahajan,[b,c,*] and Lin Xu[a,*]

[a]University of Southampton, Optoelectronics Research Centre, Faculty of Engineering and Physical Sciences, Southampton, United Kingdom

[b]University of Southampton, Institute for Life Sciences, Faculty of Environmental and Life Sciences, Southampton, United Kingdom

[c]University of Southampton, School of Chemistry, Faculty of Engineering and Physical Sciences, Southampton, United Kingdom

[d]University of Southampton, Human Development and Health, Southampton, United Kingdom

ABSTRACT. **Significance:** Precise laser ablation at the single-cell level is demonstrated on onion epidermal and human neuroblastoma cells for the first time using a 1.95 μm thulium-doped fiber laser (TDFL). The high-precision laser ablation demonstrated paves the way for micro-dissection and surgery in scientific and clinical applications.

Aim: We aimed to ablate individual target cells with pulsed laser radiation while minimizing damage to neighboring cells and to study the effects of pulse variation on laser ablation outcome.

Approach: An advanced 1.95 μm nanosecond-pulsed TDFL is developed offering a high degree of pulse control and coupled to a microscope to enable simultaneous ablating and monitoring. A reflective microscope objective is used to focus the light onto the sample without chromatic aberrations. Systematic studies of ablation outcomes using different pulse parameters are then performed.

Results: Single-cell ablation is achieved, with a precision of 31.3 ± 0.1 μm for onion epidermal cells and 20 μm for fixed human neuroblastoma cells, in which the latter demonstrates the ability to target fixed individual cells in a sample of up to 250,000 cells. Careful control of the pulse parameters produced ablation without carbonization and cavitation bubbles.

Conclusions: Single-cell level ablation harnessing a TDFL is clearly demonstrated on onion epidermal cells and human neuroblastoma cells. The TDFL, with an easily accessible range of wavelengths, provides significant opportunities in the field of biology and medicine for stimulation, dissection, and surgical applications.

 [DOI: 10.1117/1.OE.63.8.086102]

Keywords: precision ablation; pulse control; water absorption; thulium laser; 1950 nm

Paper 20240325G received Apr. 2, 2024; revised Jun. 13, 2024; accepted Jul. 5, 2024; published Aug. 10, 2024.

*Address all correspondence to Sumeet Mahajan, S.Mahajan@soton.ac.uk; Lin Xu, L.Xu@soton.ac.uk

†Joint first authors

0091-3286/2024/$28.00

1 Introduction

Laser ablation is a top-down process through which material is removed from a substrate following irradiation with a focused laser beam and occurs once the targeted volume has absorbed sufficient energy to result in degradation and destruction. Ever since the invention of the first laser in 1960 by Maiman,[1] there has been considerable anticipation toward the application of lasers to medicine and the potential therein to selectively destroy tissue; however, the first clinically viable techniques were not demonstrated until the 1980s.[2] As laser technology has progressed, applied systems have gradually permeated into a greater number of clinical settings such as keratoplasty[3–6] and lithotripsy.[7–10] Regarding the latter, holmium-doped yttrium aluminum garnet (Ho:YAG) lasers have been the accepted gold standard for the last two decades; however, in recent years, a new challenger has emerged in the form of the thulium (Tm)-fiber laser. Tm fiber lasers target peaks within the water absorption spectrum, taking advantage of the high percentage of water in the human body. The advantage the thulium-doped fiber laser (TDFL) brings is a more than four-fold increase in the water absorption coefficient, from 30 to 140 cm^{-1} as shown in Fig. 1. A higher coefficient of water absorption results in a greater ablation efficiency and lowers the ablation threshold, leading to an improved outcome for patients and, critically, an enhanced safety profile. If we consider biological tissue as turbid, scattering media,[11] lasers operating in the near and shortwave infrared (NIR, SWIR) benefit from deep penetration as compared to visible radiation[12] due to a decrease in the scattering coefficient with increasing wavelength.[13–15] Reduced attenuation thus would aid ablation efficiency by minimizing collateral heating and damage to surrounding, healthy tissues as a greater proportion of photons reach the intended target.

In comparison to bulky solid-state lasers, Tm-fiber lasers offer a number of advantages including compactness, robustness, and reliability. The large surface-area-to-volume ratio of fibers ensures simple and effective heat dissipation, and their high degree of flexibility allows application in otherwise awkward procedures such as ureteroscopy and intraoral surgery.[16] The highest infrared (IR) water absorption peak is centered at 2.94 μm,[17] which is therefore the most efficient ablating wavelength. However, water absorption alone omits subtleties in design and dissemination. Low-loss transmission of 2.94 μm radiation is currently only readily possible in soft-glass-based fibers, such as fluoride and sapphire fibers that display poor physical and chemical qualities compared to their silica-glass counterparts.[18,19] Maintaining a fused silica fiber design supports a commercially more affordable end-product which in the long-term would improve global user accessibility. Consequently, we have targeted the 1.9 μm absorption peak given that this is the highest water absorption peak transmissible through silica fibers.

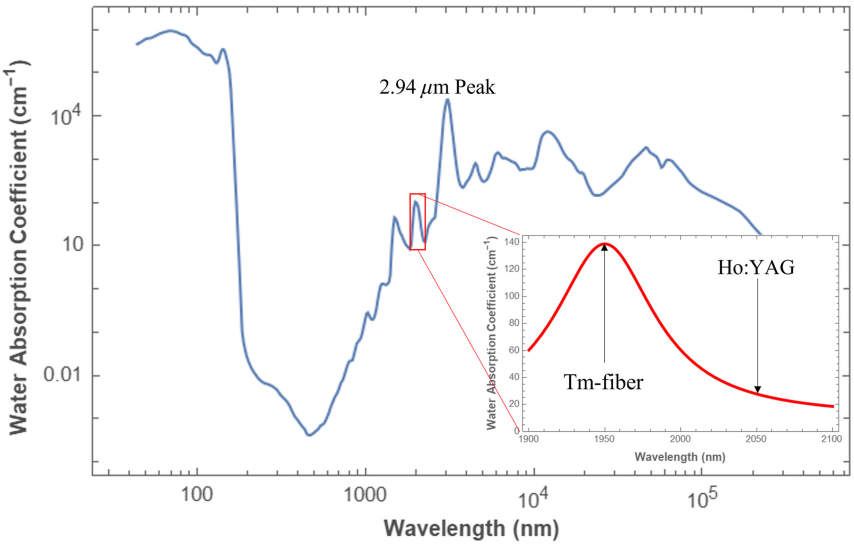

Fig. 1 Broadband water absorption spectrum ranging from the UV to the far IR with the 2.94 μm peak identified. The inset highlights the 1.95 μm peak and the difference in absorption coefficient between the Tm-fiber laser used in this investigation and a typical Ho:YAG laser.

In the quest towards minimally invasive surgery, namely cellular level precision, scientists have generally focused on systems targeting the highest peak of water absorption at 2.94 μm.[5,20,21] Utilizing 300 ps at 2.94 μm, Miller and coworkers showed that incisions with a precision of 8 μm were achievable in skin fibroblasts.[20] Achieving a similar level of precision at 1.9 μm would be a significant step forward with an alternative and more economically viable system.

A key flaw suffered by many commercial laser ablation products is their lack of control over fundamental pulse parameters. They are designed only to generate pulses with specific pulse durations and at specific repetition rates, with limited or negligible user control to customize the end result. This is a non-issue should the systems only target one type of tissue since these will be configured for a set of agreed optimum parameters from which any deviation would be damaging or dangerous.[7,22,23] Building a system for a more extensive application not only requires the targeting of a common absorption band (water) but also comprehensive control of the pulse parameters to facilitate high-quality ablation across a wide variety of tissues. The interaction between light and biological tissue is complex,[24] sensitive to both composition and morphology, and thus, any broadband laser ablation tool must be able to adapt to these changes to prove its effectiveness.

We report the development of a single-mode TDFL with a pulsed output and configured as a master oscillator power amplifier (MOPA) system. The laser output has a central wavelength of 1.95 μm, with a spectral linewidth of $\leq$0.3 nm, and provides a near-diffraction-limited output with a beam quality of $M^2 \leq 1.2$. The pulses are generated from a diode laser directly modulated by an arbitrary function generator (AFG3102, Tektronix, Beaverton, Oregon, United States). We detail the precise and effective laser ablation of two biological samples with differing morphologies: (i) onion epidermal cells and (ii) human neuroblastoma cells of the SH-SY5Y cell line. In both cases, single-cell ablation was achieved with a minimum ablation zone of 31.3 ± 0.1 μm recorded for onion epidermal cells and 20 μm for human neuroblastoma cells, representing, to the best of our knowledge, the first time laser ablation this precise has been demonstrated using a TDFL. To further understand the effects of pulsed laser emission on ablation outcome, four fundamental parameters, average power (P_{avg}), pulse duration (τ), repetition rate (R), and exposure time (t_{exp}), were individually varied using the AFG3102 and the subsequent effects on both cell types were examined.

2 Materials and Methods

2.1 TDFL Development

The TDFL has the system architecture of a MOPA, where a low-power but spectrally narrow signal is harnessed to "seed" the system with a specific wavelength, before passing through successive amplifier stages (in this case three) to reach the desired level of output power. Figure 2 shows a full schematic of the TDFL with each amplifier stage highlighted.

Electrical pulses generated using the AFG3102 were fed into an InGaAs/InP multiple-quantum-well discrete-mode laser diode (Eblana Photonics, Dublin, Ireland)[25] that was biased below the threshold, creating the desired 1.95 μm optical pulses via electrical modulation. The seed laser was actively cooled with a thermoelectric cooler (TEC) during operation to ensure a stable emission wavelength. The output power from the laser diode ($\sim$1 mW) was amplified in a pre-amplifier that consisted of an 8 m length of TDF (TmDF200, OFS). The TDF was forward core-pumped by an in-house constructed erbium-ytterbium fiber laser (EYFL) operating at 1564 nm through a wavelength division multiplexer (WDM). An isolator was placed after the seed laser to prevent any back reflection from the amplifier from damaging the seed laser. An average power of 265 mW was obtained from the pre-amplifier.

A booster amplifier was constructed based on a TDF cladding-pumped by a 9 W 793 nm laser diode (I5F-HS1, DILAS, Tucson, Arizona, United States). The double-clad TDF (PM-TDF-10P/130-HE, Coherent, East Granby, Connecticut, United States) had a core/cladding diameter of 10/130 μm, a cladding absorption of 9.6 dB/m at 793 nm, and a length of 2 m. This length of TDF was chosen to ensure sufficient pump absorption. A polarization-dependent circulator was employed to act both as an isolator and a port to monitor the backward-traveling signal for signs of stimulated Brillouin scattering (SBS)[26–28] occurring during power amplification. SBS is a

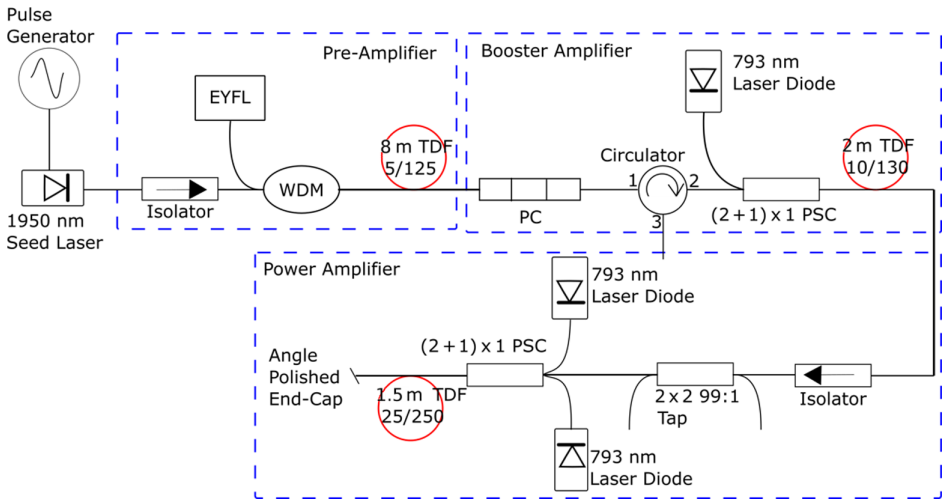

Fig. 2 Full system schematic of the TDFL with each amplifier stage contained within a dashed-line box. The 1.95 μm laser diode acts as a seed for the signal wavelength and the pulse generator ensures a broad modality of pulsed operation. The pre-amplifier stage consists of an isolator, a WDM, and an 8 m TDF with core/cladding specifications of 5/125 μm pumped by a 1565 nm EYFL. The booster amplifier consists of a polarization controller, a circulator, and a 2 m TDF with core/cladding specifications of 10/130 μm pumped by a 793 nm laser diode. The power amplifier consists of an isolator, a 2×2 99:1 tap, a 1.5 m TDF pumped by a pair of 793 nm laser diodes, and an angle-polished endcap.

nonlinear scattering effect capable of generating backward-traveling pulses with the potential to damage components within the TDFL when the optical power becomes too high. Due to the narrow spectrum generated by the seed laser (<0.3 nm) and the length of pulses used (>10 ns), preventing SBS is of the utmost importance. An average power of 1.25 W was obtained from the booster amplifier without any observable SBS.

To further increase the output power, while avoiding SBS, a power amplifier consisting of a large-mode area (LMA) TDF was built. The TDF (LMA-TDF-25P/250-M, Coherent) had a core/cladding diameter of 25/250 μm with a cladding absorption of 11.4 dB/m at 793 nm. Hence, a short TDF length of 1.5 m was selected to both eliminate the likelihood of SBS and provide sufficient pump absorption. Two 793 nm laser diodes (MTAB00107 and MTAB00114, BWT, Beijing, China) each with a maximum power of 30 W were employed to pump the TDF using a $(2+1) \times 1$ pump/signal combiner. The TDF was wired on a racetrack mount to exclude high-order modes and ensure fundamental-mode operation, and water cooling at 12°C was applied to the mount to improve and maintain the slope efficiency. An angle-polished endcap made from a 1 mm length of coreless fiber was spliced to the end of the TDF to prevent back reflection. A 2×2 coupler with a 99:1 ratio was placed behind the TDF to provide a 1% coupling port for monitoring both the forward and backward signal powers within the amplifier.

Characterization of the MOPA system (output power, spectrum, pulse shape, and beam quality) is shown in Fig. 3. Applying 50 ns pulses with a repetition rate of 250 kHz, the signal power from the power amplifier increased linearly with the pump power resulting in a slope efficiency of 40% and reaching a maximum power of 11 W as shown in Fig. 3(a). The spectrum shows a central wavelength of 1951.5 nm with an optical signal-to-noise ratio (OSNR) of 22 dB with respect to the peak of spontaneous emission background. The inset of Fig. 3(b) shows the spectrum having a narrow linewidth of ≤0.3 nm. The pulse width and repetition rate can be flexibly varied using the AFG3102 with optical pulses of 7 ns, 40 ns, 350 ns, and 680 ns shown in Fig 3(c). They are the result of electrical pulses with respective durations of 10 ns, 50 ns, 500 ns, and 1 μs. The 20 to 30% shortening of pulse duration is caused by the spiking inherent to the gain modulation of the setup.[29,30] The beam quality was measured and is shown in Fig. 3(d), exhibiting an average M^2 of <1.2. The near diffraction-limited beam quality is important to enable high-precision laser focusing for the single-cell ablation.

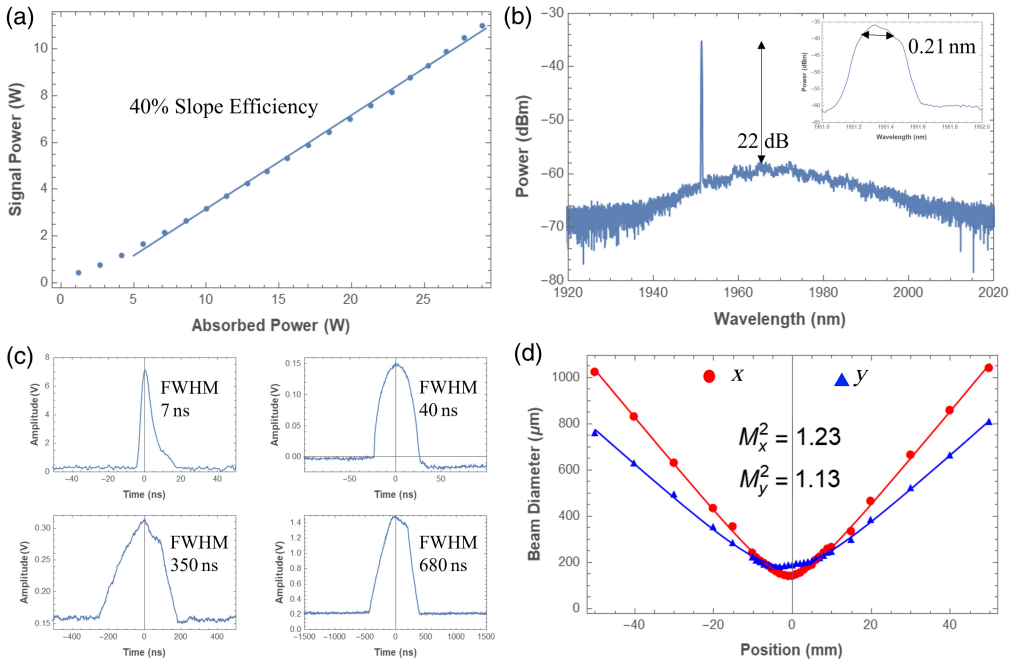

Fig. 3 (a) Power characterization of the TDFL, showing a slope efficiency of 40%. (b) A broad spectrum of the TDFL showing 22 dB OSNR with the inset showing the narrow spectrum and ≤0.3 nm linewidth (measured at 0.05 nm resolution). (c) The optical pulse shape and FWHM of a 10 ns electrical pulse (top left), 50 ns electrical pulse (top right), 500 ns electrical pulse (bottom left), and a 1 μs electrical pulse (bottom right) as measured with a photodiode. (d) The beam quality of the signal along the *x*-axis (red) and *y*-axis (blue) with a beam quality of 1.18.

The individual pulse energy (E_p) is given by the expression

$$E_p = \frac{P_{\text{avg}}}{R}, \tag{1}$$

where P_{avg} is the average power of the pulse and R is its repetition rate. The peak pulse power (P_p) is given by the expression

$$P_p = \frac{P_{\text{avg}}}{R\tau}, \tag{2}$$

where τ is the pulse duration and other symbols have their previously defined meanings. The corresponding pulse energy (E_p) and peak pulse power (P_p) for the 40 ns pulse in Fig. 3(c) are 43 μJ and 457 W, respectively.

2.2 Beam Delivery and Optimization

A beam delivery setup was designed and built, for which four essential requirements were considered. Namely, (i) the sample must be mounted in a precisely adjustable manner, (ii) the sample needs to be monitored in real-time during the ablation process, (iii) the laser beam should be focused to a suitably small spot size, and (iv) the focusing beam should be precisely positioned on the surface of each biological sample. To fulfill the first two requirements an inverted microscope (Nikon Eclipse Ti-U) was chosen as a mount for the biological samples. The microscope was equipped with a motorized stage to facilitate precise XY sample scanning (MIV-2000 TE2000HE, coupled to MS 2000 control unit, Applied Scientific Instrumentation, Eugene, Oregon, United States), with stage positions controlled via Micro-Manager 1.4 software (μManager). Brightfield microscopic images were captured using a scientific camera (Digital Sight DS-Fi1c, Nikon, Tokyo, Japan) via proprietary software (NIS Elements F, Nikon), allowing observation of the samples before, during, and after ablation. Video-rate footage of laser ablation was captured with screen recording software. Figure 4 shows the schematic of the beam delivery system which effectively delivered light from the TDFL to the sample.

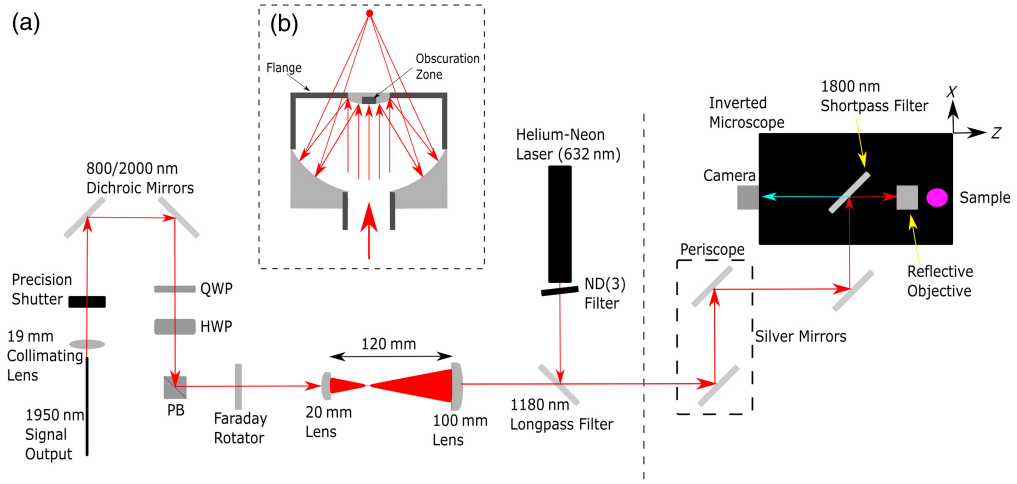

Fig. 4 (a) Schematic of the beam delivery setup that couples the 1.95 μm signal from the TDFL into the microscope for laser ablation. The signal passes through a 19 mm collimating lens and a time-controlled shutter before reflecting off a pair of 800/2000 nm dichroic mirrors. It is then transmitted through a quarter-wave plate (QWP) and a half-wave plate (HWP), where the appropriate polarization is reflected onwards through a polarization beamsplitter (PB). After passing through a Faraday rotator the beam is expanded by a pair of plano-convex lenses in a telescopic configuration. An 1180 nm longpass filter transmits the signal wavelength while additionally reflecting a He-Ne beam into a periscope comprised of two silver mirrors. A third silver mirror reflects the light into the microscope, indicated by a black box, where an 1800 nm shortpass filter reflects through a reflective objective lens and onto the sample, all while being recorded by a camera. (b) Schematic of the reflective objective. Light enters via an aperture, diverges off the smaller secondary mirror, and subsequently converges off the primary mirror. An obscuration zone of 17% is present in the objective.

A plano-convex lens with a 19 mm focal length was used to collimate the output beam from the TDFL. A time-controlled shutter (ThorLabs SH1, Newton, New Jersey, United States, connected to SC10 benchtop controller) was used to control the exposure time of the laser beam on the sample. The opening time of the shutter can be controlled with millisecond precision. A pair of 800/2000 nm dichroic mirrors filtered out the residual pump light, ensuring that only the 1.95 μm signal reached the sample, which improved the ablation quality. A quarter-wave plate (QWP) and a half-wave plate (HWP) served to adjust the output beam polarization prior to encountering a polarization beamsplitter (PB) and a Faraday rotator. The PB and Faraday rotator allowed a single linear polarization to pass through and prevented any back reflections of the same polarized light from any optical surface, protecting the amplifier from any possible damage. The telescope comprised a pair of plano-convex lenses with suitable anti-reflection (AR) coatings and expanded the beam size such that it matched the back aperture of the reflective objective, enabling tight focusing for precise laser ablation. A 100 to 20 mm focal length ratio expanded the beam diameter by a factor of 5. An 1180 nm longpass (LP) filter was placed to transmit the 1.95 μm beam into a series of silver mirrors that diverted the beam into the back aperture of the microscope. An 1800 nm shortpass (SP) filter inside the microscope reflected the signal up through the objective and onto the sample.

The 1180 nm LP filter (DMLP1180R, ThorLabs) additionally reflected an attenuated 632 nm beam from a helium-neon (He-Ne) guidance laser. The He-Ne beam was overlapped with the TDFL beam to aid and optimize alignment, with the beam paths centered within the field of view of the microscope eyepiece and brightfield camera. The LP filter permitted 89% transmission at 1.95 μm and 31% reflectance at 632 nm. The 1800 nm SP filter (DMSP1800R, ThorLabs) served two purposes; in addition to reflecting both the signal and guidance beams, there was a percentage transmission in the visible, allowing the brightfield camera to monitor the sample during ablation. This enabled the recording of video-rate ablation footage and enhanced our understanding of the photo-dynamic process. The SP filter had a reflectance of 99% at 1.95 μm, 84.5% at 632 nm, and several transmission peaks between 30 and 40% in the visible region, favoring shorter wavelength blue light.

The latter two requirements were fulfilled using a reflective objective (50102-02, Newport, Irvine, California, United States), with a reverse Cassegrain architecture [Fig. 4(b)], 36× magnification, infinite back focal length, and 0.52 NA. Using this objective, based on the beam quality, wavelength, and NA of the input laser beam, the theoretical diffraction-limited laser spot size was calculated to be 3.32 μm. The physical spot size of the beam was obtained using the knife-edge method[31] and measured to be 3.61 ± 0.22 μm, which is close to the theoretical calculation and sufficiently small enough for single-cell precision. The objective mirrors were coated with Al(MgF_2) giving a broad operating bandwidth and a reflectance of 94% at 1.95 μm. We used a reflective objective to focus both lasers on the sample to avoid any chromatic aberrations and thus ensure the coincidence of the signal focal spot and the guidance focal spot with the surface of all samples. The overall laser power transmission of this setup, from fiber output to sample, was 33%.

2.3 Sample Preparation

2.3.1 *Onion epidermal cells*

Water-rich epidermal cells within the interfacial layer between fleshy leaves of red onions were prepared to produce water-rich cell samples with high regularity. Here, samples took the form of an onion peel, i.e., intact and hydrated skin leaves (membranous layer) which contain a natural cell monolayer, with a grid-like structure, which proved helpful to elucidate ablation efficiency and collateral damage. Fresh onion skin leaves were mounted between thin coverslips (Agar Scientific, ∅24 mm, 0.13 to 0.16 mm thick) and sealed in a metal sample holder. Onions were stored at room temperature, and the onion peel cell samples were mounted on the inverted microscope stage and discarded after each experiment.

2.3.2 *Human neuroblastoma cells*

Human cell samples were cultured from the SH-SY5Y neuroblastoma cell line to produce samples with photomechanical and clinical relevancy. The SH-SY5Y cells were cultured in Dulbecco's modified Eagle's medium (DMEM), supplemented with 10% fetal bovine serum (FBS) and 1% penicillin and streptomycin (pen-strep) antibiotic mixture. Cells were incubated under standard atmospheric conditions of 37°C and 5% CO_2, monitored for mycoplasma, and passaged as required. Cells were cultured onto thin coverslips (Agar Scientific, ∅20 mm, 0.13 to 0.16 mm thick) to high confluence, around 90%, equivalent to ∼250,000 cells per well. This produced cell monolayers, which were subsequently fixed in 4% paraformaldehyde (PFA), before being washed twice with phosphate buffer solution (PBS). Samples were stored refrigerated and immersed in PBS.

For mounting onto the inverted microscope stage, the coverslips holding the cell monolayers were removed from the PBS and placed face down, sandwiched between two ∅24 mm coverslips, and placed in a metal sample holder. After the addition of PBS, the sample was sealed within the holder. Practically, this geometry ensured the laser was incident on the cell sample having only passed through one thin coverslip. The cells remained hydrated with membranes intact and stable at room temperature and in a fixed focal plane comparable to the rigid positioning of structured cells in a mature tissue sample.

2.4 Quantification of Ablation

2.4.1 *Ablation metrics*

To facilitate consistent methodology for quantifying the effect of laser ablation with varying pulse parameters on different tissue types, the following ablation metrics are defined:

1. Ablation area (AA), fully denatured/vaporized region of tissue.
2. Thermally altered area (TAA), total area of thermally irreversible damage.
3. Mechanically altered area (MAA), translated/perturbed area of tissue.
4. Ablation efficiency (AE) in percent, ratio of AA/TAA multiplied by 100.

Measurement and calculation of each metric was carried out using the widely used open-source image analysis software ImageJ (FIJI[32]), on images scaled using microscopy standards. The methodology for measuring and describing AA for neuroblastoma cells is described in Appendix Fig. 15, detailing how indicative ablation area was determined through observing cell fate during laser exposure. Brightfield images were captured using a scientific camera (Digital Sight DS-Fi1c, Nikon) mounted to the microscope side port, with proprietary software (NIS Elements F, Nikon). Video frames captured around the moment of ablation were analyzed to accurately track the cell fate following laser exposure. Video-rate footage was captured at 12 fps using screen capture software (Bandicam, Irvine, California, United States), with individual frames exported and timestamped.

For onion epidermal cells, AA described regions fully vaporized, and TAA described regions discolored due to thermal damage (brown to black). MAA was not calculated for the onion epidermal cells as their morphology rendered such effects negligible.

For human neuroblastoma cells, where thermal damage (carbonization) was not observed, AA described affected regions of cells resulting in full or partial cell bursting (evidenced by cell debris or malformation) and MAA described the area over which the beam exerts significant mechanical influence, measured as the maximal radial movement or disturbance of cells centered at the point of ablation. The MAA was mitigated by placing the sample among coverslips to ensure cells were not displaced by the pressure wave caused by an incident laser pulse before experiencing thermal influence. This was favored to enable a model conducive to the ablation of cells in a mature, structured tissue. Thus, AE was not calculated for laser ablation of human neuroblastoma cells.

2.4.2 *Cell membrane staining*

Cell membrane integrity was examined as a proxy for viability as preserved, fixed cells were examined that offer a thermomechanical model of human tissue. Trypan Blue staining was undertaken to highlight cells with damaged membranes to verify ablation effects.

Cells were stained in well plates (250,000 cells in 1 ml media) before mounting for ablation, then observed for up to 5 min following ablation to allow the stain to enter any compromised membrane. Full-color brightfield images before, immediately post-ablation, and 5 min after ablation were analyzed to observe any physical changes and any color changes due to the stain entering damaged cells over time.

3 Results

The research focused on the four fundamental pulse parameters (P_{avg}, t_{exp}, τ, R) and how their variation affected the AA, TAA, MAA, and most importantly, the AE. This process was performed on two different biological samples: onion epidermal cells and human neuroblastoma cells.

3.1 Onion Epidermal Cells

Onion epidermal cells were chosen as an experimental sample due to their repetitive grid-like nature, allowing straightforward identification of which cells were ablated, thermally altered, and unaffected. This simple morphology helped to optimize the alignment of the beam delivery system, ensuring effective and precise ablation of any future samples (i.e., human neuroblastoma cells).

Figure 5 shows the results after laser irradiation of onion epidermal cells when P_{avg} was increased from 0.85 W (a), 1.7 W (b), and 3.7 W (c), while the other parameters remained unchanged. The respective ablation efficiencies were 0.0%, 26.6% ± 1.4%, and 27.3% ± 1.4%. The final value appears a clear overestimation as the TAA shows no visible edge to the damage within the field of view. Figure 5 also shows the results after laser irradiation of onion epidermal cells when t_{exp} was decreased from 1 s (d), 0.75 s (e), and 0.5 s (f), while the other parameters remained unchanged. The respective ablation efficiencies were 33.2% ± 1.5%, 22.1% ± 1.6%, and 46.9% ± 3.9%.

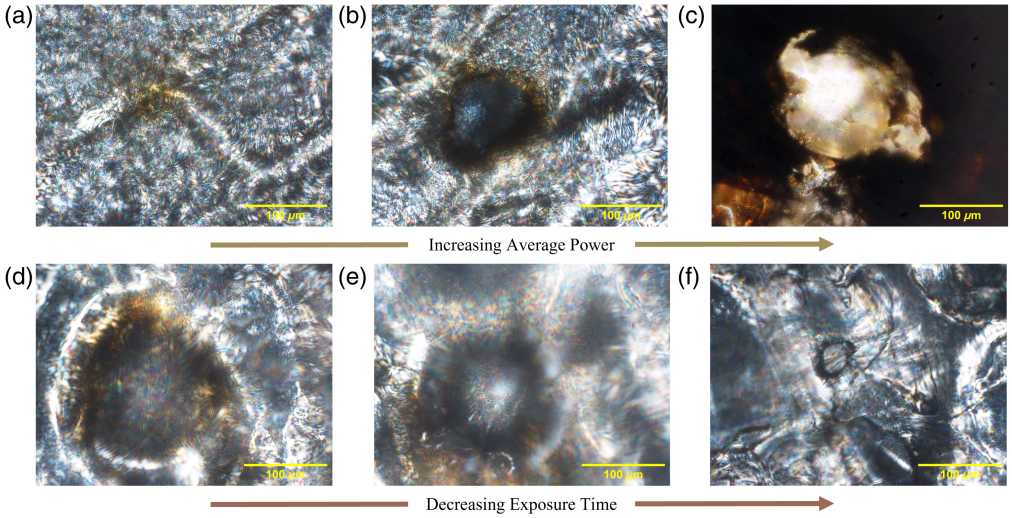

Fig. 5 Establishing ablation efficiencies (AE) with increasing average power (P_{avg}) and decreasing exposure time (t_{exp}) on onion epidermal cells. The top row describes the affected area under (a) $P_{avg} = 0.85$ W, (b) $P_{avg} = 1.7$ W, and (c) $P_{avg} = 3.7$ W pulses. Respective AE was recorded as 0.0%, 26.6% ± 1.4%, and 27.3% ± 1.4%. The remaining pulse parameters were fixed at $t_{exp} = 5$ s, $\tau = 40$ ns, and $R = 250$ kHz. The bottom row describes the affected area under (d) $t_{exp} = 1$ s, (e) $t_{exp} = 0.75$ s, and (f) $t_{exp} = 0.5$ s pulses. Respective AE was recorded as 33.2% ± 1.5%, 22.1% ± 1.6%, and 46.9% ± 3.9%. The remaining pulse parameters were fixed at $P_{avg} = 3.7$ W, $\tau = 40$ ns, and $R = 250$ kHz. Scale bar = 100 μm.

Figure 6 shows the results after laser irradiation of onion epidermal cells when τ was increased from 40 ns (a), 350 ns (b), and 680 ns (c), while the other parameters remained unchanged. The respective ablation efficiencies were 46.9% ± 3.9%, 25.7% ± 1.0%, and 18.0% ± 0.9%. Figure 6(c) shows such widespread damage that it extends beyond the field of view, affecting the calculated AE value. Figure 6 also shows the results after laser irradiation

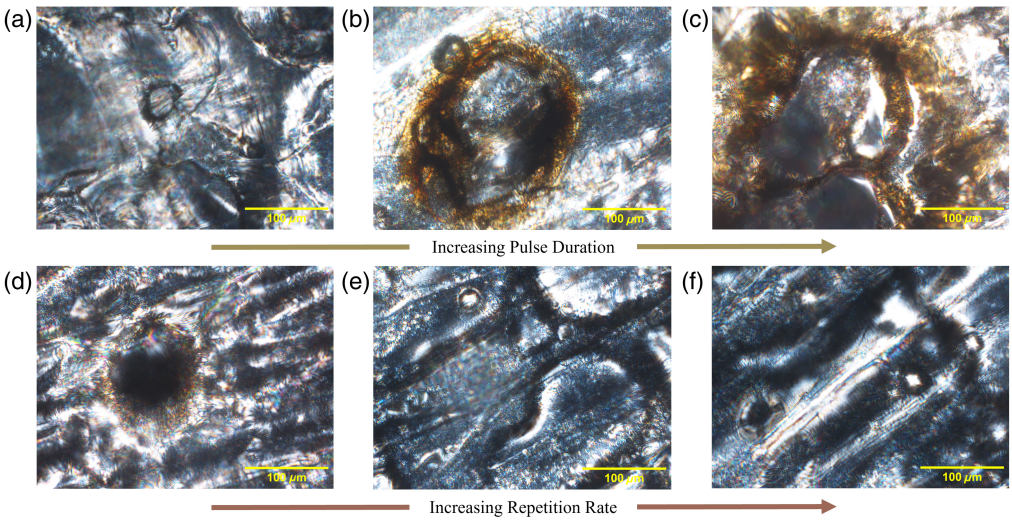

Fig. 6 Establishing ablation efficiencies (AE) with increasing pulse duration (τ) and repetition rate (R) on onion epidermal cells. The top row describes the affected area under (a) $\tau = 40$ ns, (b) $\tau = 350$ ns, and (c) $\tau = 680$ ns pulses. The respective AE was recorded as 46.9% ± 3.9%, 25.7% ± 1.0%, and 18.0% ± 0.9%. The remaining pulse parameters were fixed at $P_{avg} = 3.7$ W, $t_{exp} = 0.5$ s, and $R = 250$ kHz. The bottom row describes the affected area under (d) $R = 1.25$ MHz, (e) $R = 2.5$ MHz, and (f) $R = 5.0$ MHz pulses. The respective AE was recorded as 45.3% ± 3.9%, 0.0%, and 0.0%. The remaining pulse parameters were fixed: $P_{avg} = 3.7$ W, $t_{exp} = 0.5$ s, $\tau = 7$ ns. Scale bar = 100 μm.

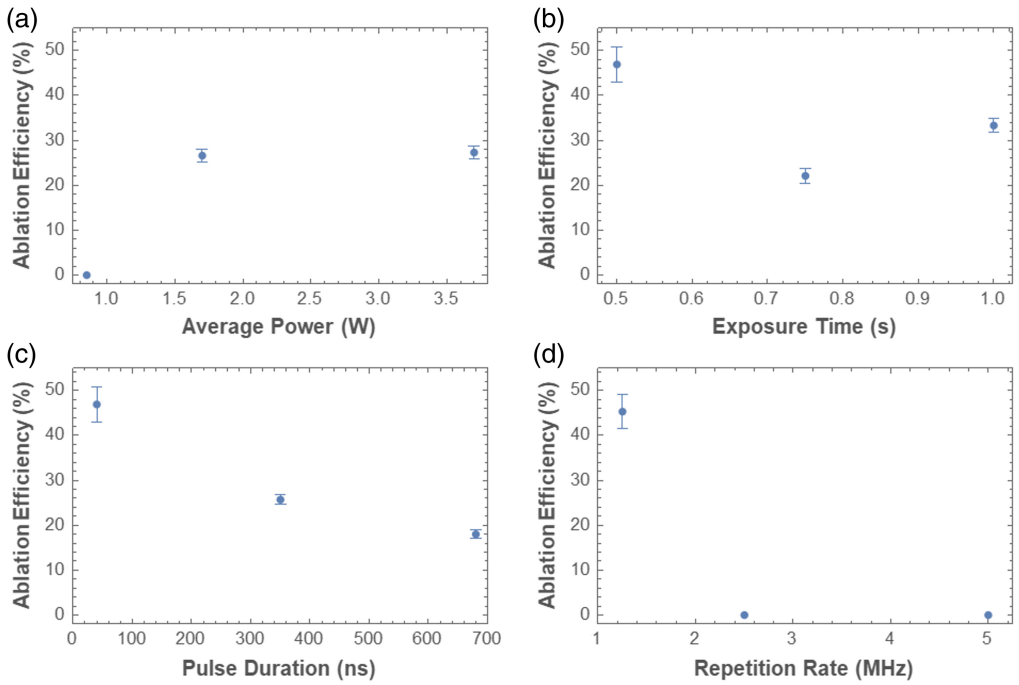

Fig. 7 Influence of each pulse parameter in isolation against the subsequent AE on onion cells. The relationship between AE and (a) average power, P_{avg}; (b) exposure time, t_{exp}; (c) pulse duration, τ; and (d) repetition rate, R, is shown. For each test, optimal values for the remaining pulse parameters were determined by those which gave the highest precision and kept constant for subsequent tests.

of onion epidermal cells when R was increased from 1.25 MHz (d), 2.5 MHz (e), and 5 MHz (f), while the other parameters remained unchanged. The respective ablation efficiencies were $45.3\% \pm 3.9\%$, 0.0%, and 0.0%.

Figure 7 depicts the variation of AE with respect to each of the four fundamental pulse parameters.

3.2 Human Neuroblastoma Cells

Fixed human neuroblastoma cells of the cloned SH-SY5Y cell line were examined to show the viability of precisely ablating cancer cells with a laboratory-based pre-clinically relevant model. Practically, SH-SY5Y cells are easy to work with since the culturing process is robust and straightforward. Once cultured, the cells exist in a highly confluent monolayer, better emulating the closely packed cells together *in vivo*, thereby providing samples to demonstrate high selectivity and precision ablation. Variation of the pulse parameters enabled us to target and ablate individual cells in samples containing up to 250,000 cells. The white circles in Figs. 8-11 represents the indicative AA for each different pulse modality used.

Figure 8 shows the before and after images following the laser irradiation of human neuroblastoma cells when t_{exp} was decreased from 0.5 s [(a)–(b)], 0.3 s [(c)–(d)], and 0.1 s [(e)–(f)], while the other parameters remained unchanged. The respective AA values were $33895 \pm 98\ \mu m^2$, $26733 \pm 256\ \mu m^2$, and $6783 \pm 23\ \mu m^2$. The data is quantitated in Fig. 12.

Figure 9 shows the before and after images following the laser irradiation of human neuroblastoma cells when P_{avg} was increased from 0.39 W [(a)–(b)], 1.7 W [(c)–(d)], and 3.7 W [(e)–(f)], while the other parameters remained unchanged. The respective AA values were $435 \pm 16\ \mu m^2$, $10{,}904 \pm 89\ \mu m^2$, and $31{,}553 \pm 236\ \mu m^2$. The data is quantitated in Fig. 12.

Figure 10 shows the before and after images following the laser irradiation of human neuroblastoma cells when τ is increased from 7 ns [(a)–(b)], 40 ns [(c)–(d)], and 350 ns [(e)–(f)], while the other parameters remained unchanged. The respective AA values were $512 \pm 10\ \mu m^2$, $2833 \pm 21\ \mu m^2$, and $9099 \pm 69\ \mu m^2$. The data is quantitated in Fig. 12.

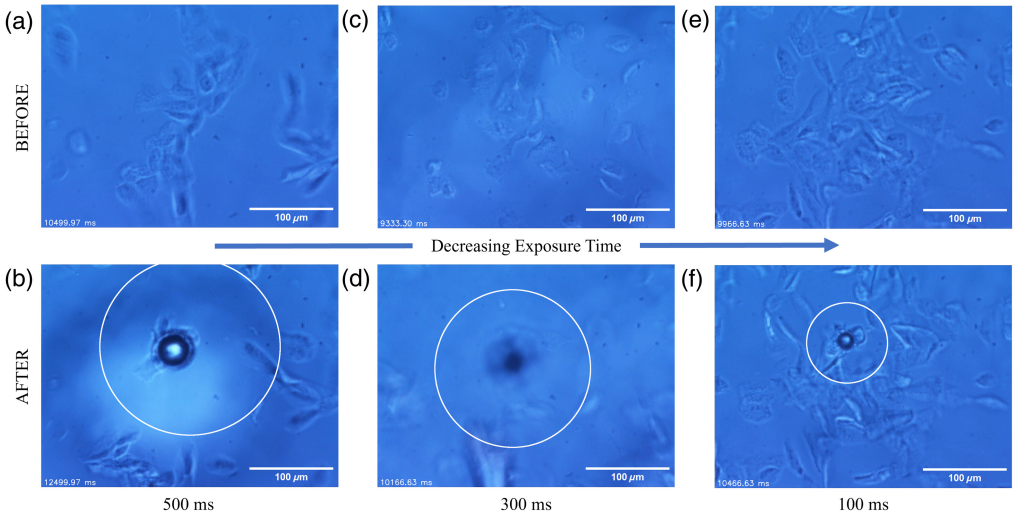

Fig. 8 Increasing ablation precision with decreasing exposure time (t_{exp}) on SH-SY5Y human neuroblastoma cells. Panel (a) shows before and (b) after ablation with $t_{exp} = 500$ ms; (c) panel shows before and (d) after ablation with $t_{exp} = 300$ ms; panel (e) shows before and (f) after ablation with $t_{exp} = 100$ ms. The remaining pulse parameters were fixed at $P_{avg} = 0.87$ W, $\tau = 7$ ns, and $R = 1.25$ MHz. Scale bar = 100 μm.

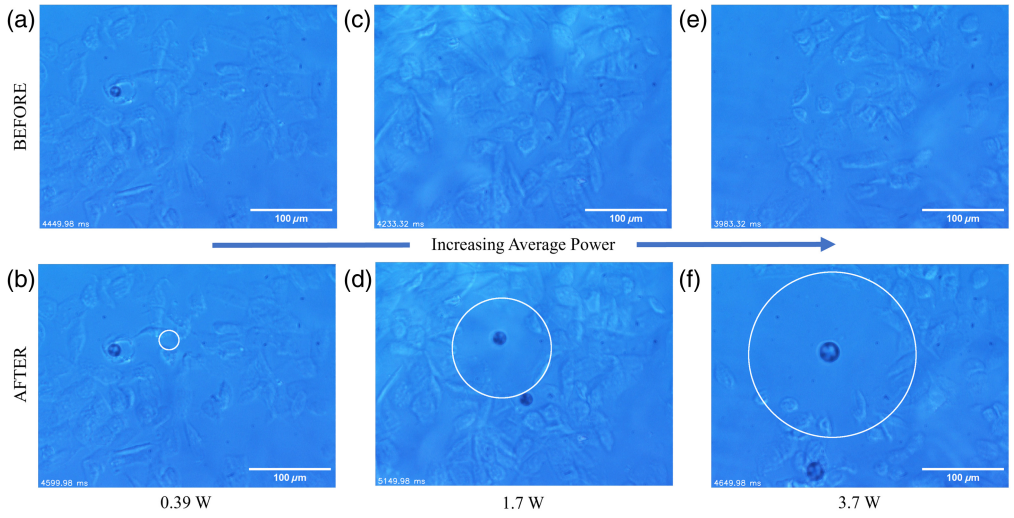

Fig. 9 Decreasing ablation precision with increasing average power (P_{avg}) on SH-SY5Y human neuroblastoma cells. Panel (a) shows before and (b) after ablation with $P_{avg} = 0.39$ W; panel (c) shows before and (d) after ablation with $P_{avg} = 1.7$ W; and panel (e) shows before and (f) after ablation with $P_{avg} = 3.7$ W. The remaining pulse parameters were fixed at $t_{exp} = 0.1$ s, $\tau = 7$ ns, and $R = 1.25$ MHz. Scale bar = 100 μm.

Figure 11 shows the before and after images following the laser irradiation of human neuroblastoma cells when R is increased from 1.25 MHz [(a)–(b)], 5.0 MHz [(c)–(d)], and 20.0 MHz [(e)–(f)], while the other parameters remained unchanged. The respective AA values were 517 ± 13 μm^2, 1167 ± 18 μm^2, and $19{,}153 \pm 191$ μm^2. The data is quantitated in Fig. 12.

Figure 12 displays the quantitative trends for AA with the different pulse parameters investigated in this work. Optimal values for a given parameter were determined by that which gave the highest precision (smallest AA) and kept constant for subsequent tests. The ideal parameters for precise ablation of the SH-SY5Y samples were determined to be $P_{avg} = 0.25 - 0.32$ W, $t_{exp} = 0.5$ s, $\tau = 7$ ns, and $R = 1.25$ MHz. This allowed accurate ablation of a single cell, which was verified with a cell viability assay.

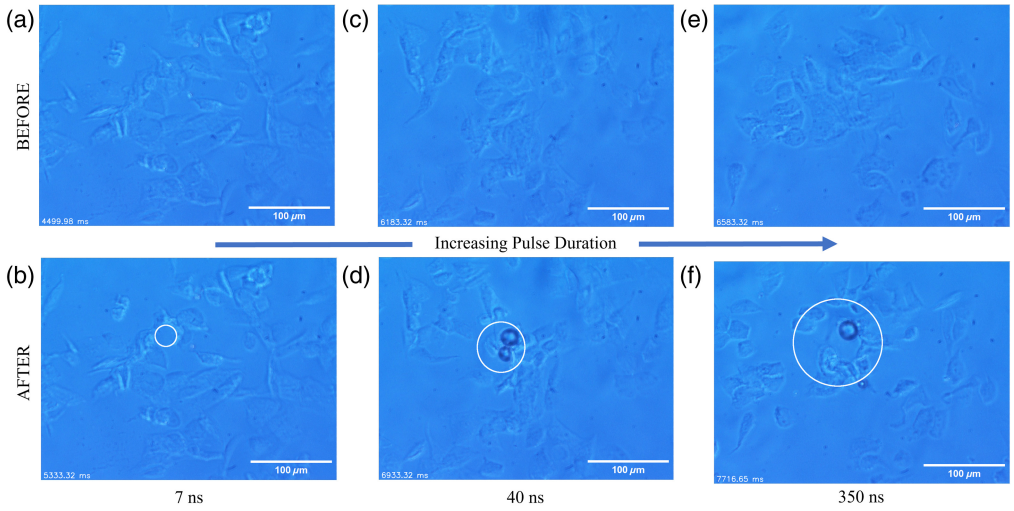

Fig. 10 Decreasing ablation precision with increasing pulse duration (τ) on SH-SY5Y human neuroblastoma cells. Panel (a) shows before and (b) after ablation with $\tau = 7$ ns; panel (c) shows before and (d) after ablation with $\tau = 40$ ns; and panel (e) shows before and (f) after ablation with $\tau = 350$ ns. The remaining pulse parameters were fixed: $P_{avg} = 0.32$ W, $t_{exp} = 0.5$ s, and $R = 1.25$ MHz. Scale bar $= 100$ μm.

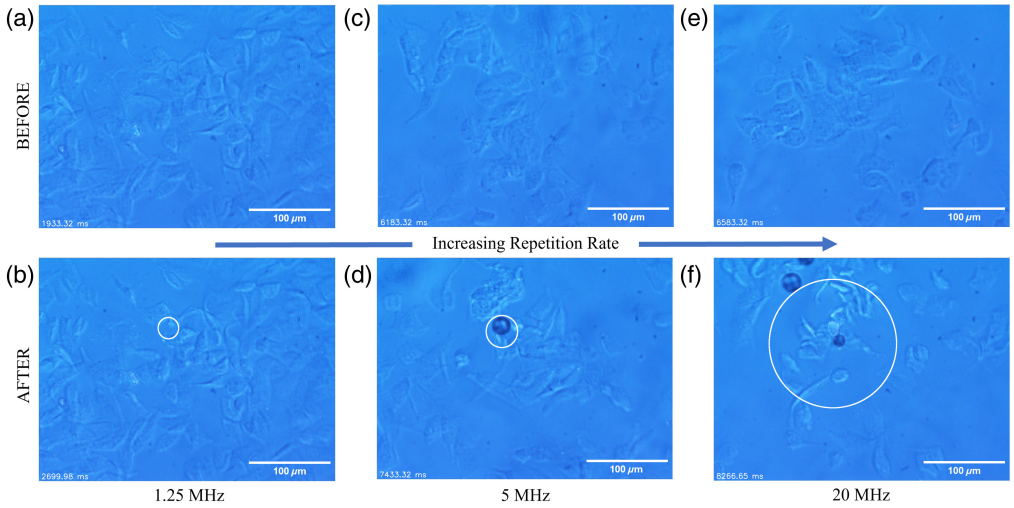

Fig. 11 Decreasing ablation precision with increasing repetition rate (R) on SH-SY5Y human neuroblastoma cells. Panel (a) shows before and (b) after ablation with $R = 1.25$ MHz; panel (c) shows before and (d) after ablation with $R = 5.0$ MHz; panel (e) shows before and (f) after ablation with $R = 20.0$ MHz. The remaining pulse parameters were fixed: $P_{avg} = 0.32$ W, $t_{exp} = 0.5$ s, and $\tau = 7$ ns. Scale bar $= 100$ μm.

3.3 Single Cell Precision

Figure 13 shows fixed single isolated human neuroblastoma cells having undergone significant mechanical damage under the ablating beam, while the surrounding cells remain unaffected. Ablation was carried out with parameters of $P_{avg} = 0.25$ W, $t_{exp} = 0.5$ s, $\tau = 7$ ns, and $R = 1.25$ MHz. AA was quantified as 405 ± 12 μm^2 [Figs. 13(a)–13(b)] and 311 ± 3 μm^2 [Figs. 13(c)–13(d)], and as a result, the respective ablation precision demonstrated is 22.7 ± 0.1 μm and 19.9 ± 0.1 μm. "Debris" of the ablated cell is visible, showing that ablation power is sufficient to damage (beyond the ablation threshold) but not vaporize the tissue unduly,

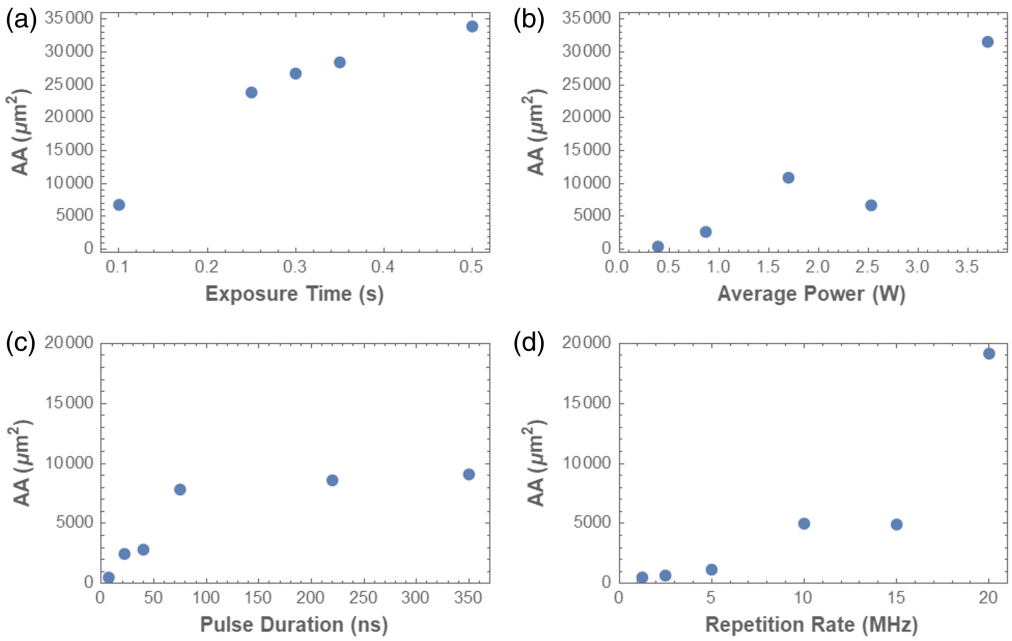

Fig. 12 Influence of each pulse parameter in isolation on ablation performance on neuroblastoma cells. The relationship between ablation area and (a) exposure time, t_{exp}; (b) average power, P_{avg}; (c) pulse duration, τ; and (d) repetition rate, R, is shown. For each test, optimal values for the remaining pulse parameters were determined by those which gave the highest precision and kept constant for subsequent tests.

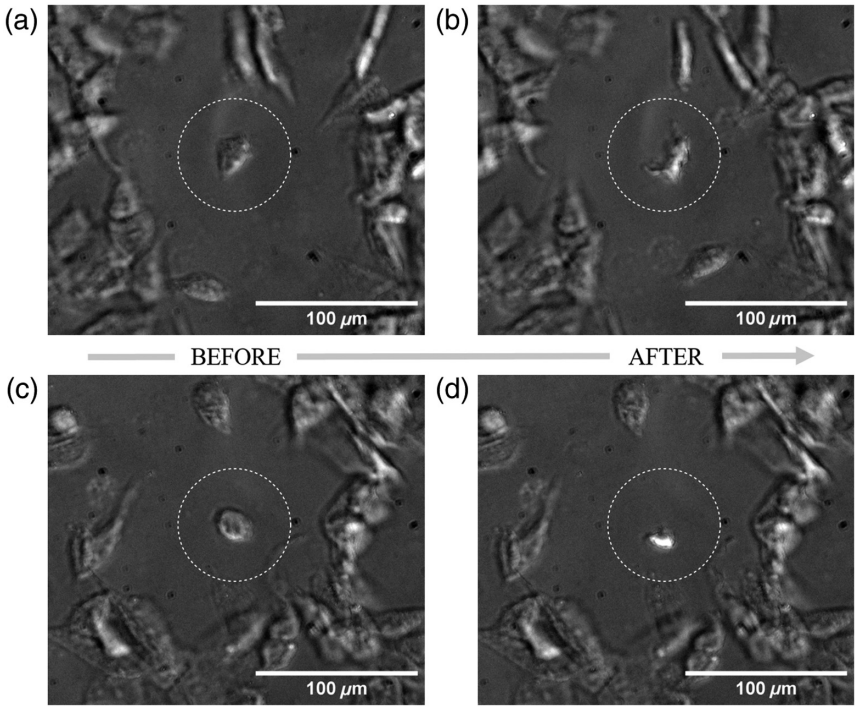

Fig. 13 Single isolated human neuroblastoma cells ablated while surrounding cells remain unperturbed. Results show the "debris" of the cell after undergoing significant mechanical damage. Ablation was carried out with parameters $P_{avg} = 0.25$ W, $t_{exp} = 0.5$ s, $\tau = 10$ ns, and $R = 1.25$ MHz on two occasions, (a)–(b) and (c)–(d). The dashed circle merely indicates which cell was targeted and is not representative of the AA value.

indicating pulse parameters have been tailored for accurate ablation with negligible collateral effect.

4 Discussion

Analysis of ablation outcomes can be carried out qualitatively (observed effects) and quantitatively (calculating AE values, as previously defined), following analysis of individual pulse parameters. Figure 5 shows the outcome when P_{avg} or t_{exp} variation in the ablation of onion epidermal cells, i.e., consequences of change in total energy deposited onto the samples. Biological tissue has a threshold of radiant exposure (ablation threshold) and delivering insufficient energy resulted in a degree of visible carbonization but no ablation as in Fig. 5(a). Increasing P_{avg} further increased the total energy deposited, crossing the threshold, and delivering subsequent ablation. However, also evident is an upper energy limit, since an excessive P_{avg} value led to widespread carbonization [Fig. 5(c)], which is undesirable. Decreasing the t_{exp} lowered the total energy deposited onto the sample (P_p was kept constant). Decreasing t_{exp} reduced both the AA and TAA until ablation with a precision of 31.3 ± 0.1 μm was achieved with an AE of $46.9\% \pm 3.9\%$, under pulse parameters of $P_{\text{avg}} = 3.7$ W, $t_{\text{exp}} = 0.5$ s, $\tau = 40$ ns, and $R = 250$ kHz. This was sufficiently small to ablate a single onion cell without visibly affecting neighboring cells and with minimal visible carbonization observed on these neighboring cells [Fig. 5(f)]. Neither the P_{avg} nor t_{exp} data yield any clear trend in AE primarily because the sample set is small. Regarding the ablation threshold, the pulse parameters used in Fig. 5(a) deposited 4.25 J of total energy onto the onion sample without ablating it, whereas the pulse parameters used in Fig. 5(f) deposited only 1.85 J of total energy onto the same tissue, but this time resulted in single-cell ablation. This is clear evidence that the total amount of energy deposited is but one part of the puzzle, and the manner in which it is deposited plays a significant, if not greater, role. Both E_p and P_p are higher in Fig. 5(f) compared to Fig. 5(a), and this suggests that delivering the energy over a shorter time scale improves ablation outcomes. Theoretically, this will increase the temperature in the targeted tissue, increasing the likelihood of tissue being ablated and vaporized.[24]

Figure 6 shows the effects of τ or R variation in the ablation of onion epidermal cells, and in each of these cases, the total deposited energy remained constant, whereas the manner in which it was deposited is changing. Increasing τ resulted in a clear trend qualitatively and quantitatively with a much larger AA and TAA visible for longer pulses and a decreasing AE value. The reduced AE can be explained by the lack of thermal confinement.[24] Each biological tissue type has a characteristic thermal diffusion time (t_d), and if $\tau \leq t_d$, then E_p will be unable to diffuse into any neighboring cells and therefore will affect only the targeted cell.[24,33] A 40 ns pulse limits the AA to a circle 31.3 ± 0.1 μm in diameter ablating only a single cell [Fig. 6(a)], whereas a 680 ns pulse of identical energy causes widespread ablation and carbonization hundreds of microns across [Fig. 6(c)]. Therefore, to reduce collateral damage, shorter pulses are favorable for achieving both high precision and high efficiency, both of which are extremely desirable for microsurgical applications. Increasing the R value of the laser pulses maintained the total energy deposited, but reduced both E_p and P_p, such that instead of a low number of high-energy pulse, there is now a high number of low-energy pulses. This change in the pulse train produced only the modest discoloration [Fig. 6(e)] or no visible changes [Fig. 6(f)]. Higher temperatures and pressure have been recorded in tissue[24] irradiated with shorter and more intense pulses; therefore, the increase in R has evidently affected the pulse to lower incident radiation below the ablation threshold. This again emphasizes that the manner in which the energy is delivered is of equal importance as to how much energy is delivered.

Figures 8 and 12(a) show the effects of t_{exp} variation in ablation on human neuroblastoma cells. There was a distinct and visible increase of AA directly alongside increasing t_{exp}. No thermal damage was visible on human neuroblastoma cells; however, mechanical effects were observed wherein cells were pushed outward from the center of the incident beam. MAA increased with t_{exp}, qualitatively evident since large areas empty of cells are visible in

Figs. 8 and 9. As with the onion epidermal cells, a shorter t_{exp} is preferable when the aim is to confine the thermomechanical effects and achieve precise ablation.

Figures 9 and 12(b) show the effects of P_{avg} variation in ablation on human neuroblastoma cells. There was an overall increase in AA with increasing P_{avg}, although the AA value dropped as P_{avg} changed from 1.7 to 2.5 W. Again, we considered cell membrane integrity as a proxy for cell damage with the preserved, dead cell models. As such, we carried out staining with Trypan Blue, which highlighted cells with intact and damaged membranes to verify collateral ablation effects. As P_{avg} increased, MAA gradually increased, which was considered as collateral damage. The dark circle present before and after in Figs. 9(a) and 9(b) is a cavitation bubble from a prior ablation experiment, and the fact that it has remained stationary through a subsequent burst of radiation is further evidence of the precision capabilities of this system when the pulse parameters are optimized. A P_{avg} value of 0.39 W [Fig. 9(b)] resulted in ablation with a precision of 23.5 ± 0.1 μm, small enough to ablate a single cell.

Figures 10 and 12(c) show the effect of τ variation in ablation on human neuroblastoma cells, and we observed an identical trend as apparent in the onion epidermal cells. The AA increased directly with increasing τ, as thermomechanical confinement worsened with longer pulses. However, above 75 ns, the rate at which the AA values increased was reduced significantly, suggesting the thermal diffusion time for human neuroblastoma cells is close to this value. A τ value of 7 ns [Fig. 10(b)] resulted in ablation with a precision of 25.5 ± 0.1 μm, sufficient to ablate a single cell. These results further emphasize the importance of short pulses for precise ablation and confining of the effects of the incident beam.

Figures 11 and 12(d) show the effect of R variation on human neuroblastoma cells, wherein we observed increasing AA with increasing R. This differed from our experiments with onion epidermal cells, most likely due to the differing morphology between the two samples. As R increased, the duty cycle of the beam became larger, and as a result, such behavior is more closely mirrored to that of a CW laser beam. As the beam becomes quasi-CW, the confinement of its thermomechanical effects is reduced, in consistent with the results observed. In Figs. 11(d) and 11(f), we observe cavitation bubbles outside the ablated area. It was observed in the video footage of these ablation tests that each cavitation bubble formed at the center of the incident beam. Some of these bubbles were then pushed outwards by the mechanical forces of the incident beam, ending up in a position outside the ablated area. This was observed with some regularity and indicated a sub-optimal choice of pulse parameter, prompting further investigation. An R value of 1.25 MHz [Fig. 11(b)] resulted in ablation with a precision of 25.6 ± 0.1 μm.

The results indicate precise cellular ablation is best achieved with short pulse durations and low repetition rates, with a radiant exposure just above the tissue threshold. A higher radiant exposure, longer pulse duration, or higher repetition rate would serve only to deposit excess energy or reduce thermomechanical confinement and thus result in a lower ablation efficiency. Ablation carried out under sub-optimal pulse parameters displayed secondary unwanted effects including the creation of large cavitation bubbles in the cell sample, which expanded under exposure, before collapsing inwards, applying further pressure to the cells. This likely induced mechanical damage to the cells, further increasing the collateral damage. These cavitation bubbles are explicitly visible as small black circles throughout Figs. 8–11. and coincide often with the beam focal spot, although they sometimes end up nearby but distinct from the ablation center [Fig. 9(d)].

The samples ablated in this investigation are essentially cell monolayers, with which we have demonstrated effective and precise lateral resolution. Regarding the resolution along the propagation direction, i.e., along the z-axis, we can calculate the depth of focus of our objective using

$$\Delta z = \frac{\lambda}{4n\left(1 - \sqrt{1 - \left(\frac{\mathrm{NA}}{n}\right)^2}\right)}, \tag{3}$$

where Δz is the depth of field, λ is the signal wavelength, NA is the objective's numerical aperture, and n is its refractive index.[34] The calculated depth of focus is 3.34 μm, and outside this

depth, the quality of ablation will decrease. Further away from the focal spot, a larger spot size could potentially affect a bigger area. However, as spot size increases, the radiant exposure will decrease, till below the ablation threshold where only carbonization will occur. The exact spot size at which this occurs will depend on the pulse parameters identified in this investigation.

Figure 14 describes single-cell scale ablation (observed with an average short axis diameter of 28.4 ± 0.1 μm) under ideal pulse parameters, employing a cell viability assay (Trypan Blue dye staining) to verify which cells are significantly damaged. A decrease in the cell membrane integrity and thus increased permeability was used as a marker for cell damage following ablation. Since fixing using PFA (protein crosslinking to stabilize the cells) does not significantly perforate the cell membranes (absence of large pore perforation), dye uptake could indicate cells sufficiently damaged upon laser irradiation. In practical terms, the cell membranes may be affected to a limited degree, allowing minimal dye uptake and resulting in some light staining before ablation, as shown in Fig 14(a).[35] In comparing the cells immediately post-ablation [Fig. 14(b)] and 300 s after ablation [Fig. 14(c)], there is increased saturation of the dye in the ablated cell tissues, indicating uptake through significantly mechanically compromised cell membranes (a marker for cell viability). Crucially, the surrounding unaffected cells show no change in morphology or dye uptake before ablation, indicating the high rate of cell survival and validating the accuracy of our ablation.

From the literature, we ascertain that to the best of our knowledge, selective ablation at the single-cell level has never been achieved before at 1.95 μm in the nanosecond pulse regime. Van Acker and colleagues[36] report on the use of a 193 nm ArF excimer laser radiation to ablate cells from the breast cancer cell lines of MDA-MB-231 X4 and MDA-MB-468 for the purposes of inductively coupled plasma-mass spectrometry. However, the smallest spot size they use is 30 μm, and they state that "selective ablation of single cells from a cluster cannot be guaranteed,"[36] something we have demonstrated above. We have shown that shorter pulses maximize thermomechanical confinement and thus improve precision, and Zhao and colleagues[37] were able to use 250 fs pulses from an 805 nm source to selectively microdissect (ablate) *Caenorhabditis elegans* neurons, which have an approximate size of <3 μm. Femtosecond pulse generation is a significantly more complex procedure compared to that of nanosecond pulse generation, and in this case, a pulse duration of five orders of magnitude lower (250 fs compared to 10 ns) results in only a one order of magnitude improvement in ablation precision (2 μm compared to 20 μm). Mangione and colleagues[38] also used femtosecond pulses to photoablate single cells in the *Drosophila* epidermis, achieving a precision of <5 μm. They also monitor their samples during and after ablation, which is essential to fully understand the effects on both the target cell and the neighboring cells.

By defining precise and selective ablation of two structurally distinct cell samples (plant and animal), we demonstrate the broad capabilities inherent to our system and any system designed to

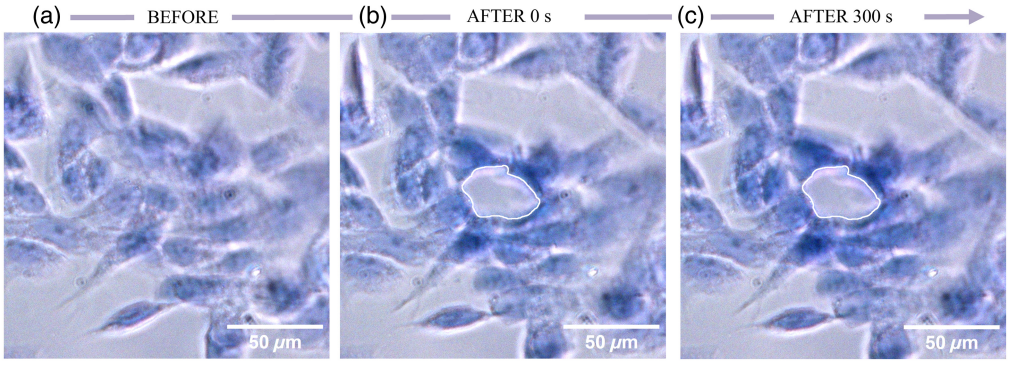

Fig. 14 Cell viability assay for single human neuroblastoma cell ablation, full-color brightfield images taken (a) before, (b) immediately after, and (c) 5 min after ablation. Ablated area boundary marked, the short axis with an average diameter of 28.4 ± 0.1 μm, of the scale of a single cell. Compromised cell membrane indicating significant damage shown by increased blue color saturation (Trypan Blue stain) in ablated cell tissue after 5 min. Ablation was carried out with parameters $P_{avg} = 0.32$ W, $t_{exp} = 0.5$ s, $\tau = 7$ ns, and $R = 1.25$ MHz.

target a common absorption band. From a clinical perspective, the preservation of healthy tissue is the highest priority; therefore, to maximize such an outcome, we intend to conduct further studies using picosecond pulses. Broadening the already ample flexibility of pulse control will undoubtedly lead to improved ablation outcomes and imbue the system itself with a greater potential.

5 Conclusion

This study demonstrates ablation with single-cell precision using a 1.95 μm TDFL on onion epidermal cells and fixed SH-5YSY human neuroblastoma cells as tissue models. Pulse parameters were progressively tuned to confine all damage (intended or collateral) to within the bounds of one target cell, and results demonstrate that short pulse durations and low pulse repetition rates work best to confine the thermomechanical effects of laser radiation, allowing minimal collateral damage to be compatible with clinical use cases. Optimizing these parameters along with average power and exposure time, ablation with a precision of 31.3 ± 0.1 μm was demonstrated on onion epidermal cells, and a precision of 19.9 ± 0.1 μm on human neuroblastoma cells. The use of a high peak pulse power combined with a low average power yielded the most precise results, and the ability to target and destroy human tissue with single-cell precision on a coverslip containing in excess of 250,000 cells is an attractive one. In conclusion, we demonstrate the capabilities of the 1.95 μm TDFL as a tool for precise and selective ablation of tissue and aim to replicate this precision on a larger scale with significant implications therein for clinical applications across a range of areas.

6 Appendix: Measurement of AA in SH-SY5Y Human Neuroblastoma Cells

Appendix Fig. 15 provides an example of how AA was quantified in SH-SY5Y human neuroblastoma cells.

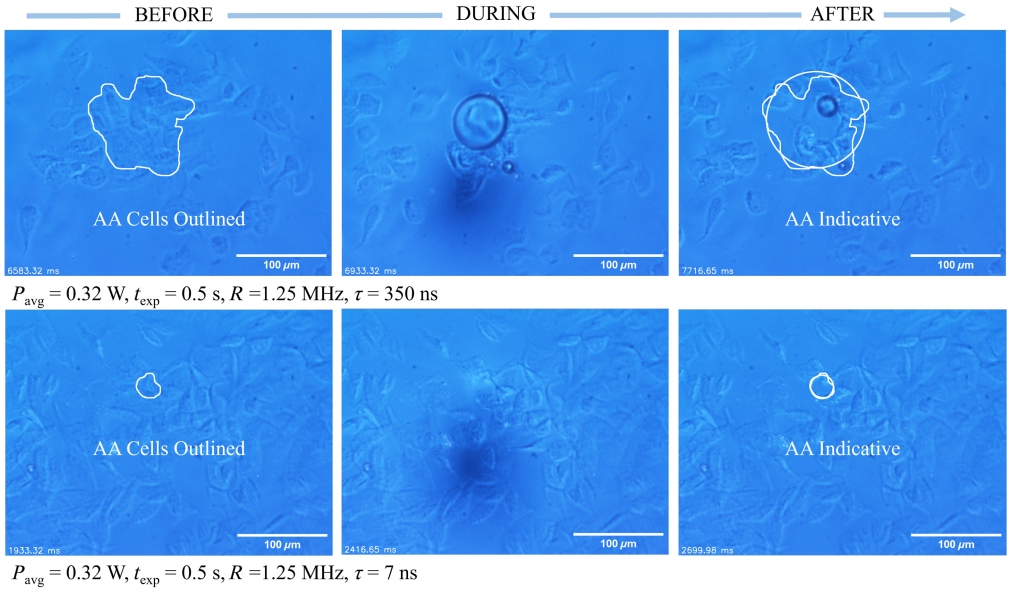

Fig. 15 Methodology for quantifying ablated area (AA): from left to right shows brightfield images captured from video footage of the cell sample immediately before, during, and after ablation. Regions of the sample considered for AA are highlighted (right) by the selection brush tool used for accurate measurements of the directly affected cells ("AA cells outlined") and are highlighted (left) as indicative areas under the influence of the symmetric beam spot ("AA Indicative").

Disclosures

The authors declare that there are no conflicts of interest related to this article.

Code and Data Availability

Data underlying the results can be found at DOI: https://doi.org/10.5258/SOTON/D3119.

Acknowledgments

This work is supported by the Engineering and Physical Sciences Research Council (EPSRC), InLightenUs Transformative Healthcare 2050 project (Grant No. EP/T020997/2); Transformative Imaging for Quantitative Biology Partnership (Grant No. EP/V038036/1); and AirGuide Photonics Programme Grant (Grant No. EP/P030181/1).

References

1. T. H. Maiman, "Stimulated optical radiation in ruby," *Nature* **187**, 493–494 (1960).
2. J. M. Krauss et al., "Laser interactions with the cornea," *Surv. Ophthalmol.* **31**(1), 37–53 (1986).
3. Q. Ren et al., "Mid-infrared laser ablation of the cornea: a comparative study," *Lasers Surg. Med.* **12**(3), 274–281 (1992).
4. A. A. Serafetinides et al., "Alternatives to excimer laser refractive surgery: UV and mid-infrared laser ablation of intraocular lenses and porcine cornea," *Proc. SPIE* **6604**, 660427 (2007).
5. S. J. Linke et al., "A new technology for applanation free corneal trephination: the picosecond infrared laser (PIRL)," *PLoS One* **10**(3), e0120944 (2015).
6. R. Deshmukh, L. J. Stevenson, and R. B. Vajpayee, "Laser-assisted corneal transplantation surgery," *Surv. Ophthalmol.* **66**(5), 826–837 (2021).
7. R. L. Blackmon, P. B. Irby, and N. M. Fried, "Comparison of holmium:YAG and thulium fiber laser lithotripsy: ablation thresholds, ablation rates, and retropulsion effects," *J. Biomed. Opt.* **16**(7), 071403 (2011).
8. D. Pal et al., "COM stone dusting and soft tissue ablation with Q-switched thulium fiber laser," *IEEE J. Sel. Top. Quantum Electron.* **25**(1), 1–8 (2019).
9. O. Traxler and E. X. Keller, "Thulium fiber laser: the new player for kidney stone treatment? A comparison with Holmium:YAG laser," *World J. Urol.* **38**(8), 1883–1894 (2020).
10. M. Taratkin et al., "How lasers ablate stones: in-vitro study of laser lithotripsy (Ho:YAG and Tm-fiber lasers) in different environments," *J. Endourol.* **35**(6), 931–936 (2020).
11. L. A. Sordillo et al., "Deep optical imaging of tissue using the second and third near-infrared spectral windows," *J. Biomed. Opt.* **19**(5), 056004 (2014).
12. L. Shi and R. R. Alfano, Eds., *Deep Imaging in Tissue and Biomedical Materials*, Jenny Stanford Publishing (2017).
13. S. Golovynskyi et al., "Optical windows for head tissues in near-infrared and short-wave infrared regions: approaching transcranial light applications," *J. Biophotonics* **11**(12), 1–12 (2018).
14. A. Bhandari et al., "Modeling optical properties of human skin using Mie theory for particles with different size distributions and refractive indices," *Opt. Express.* **19**(15), 14549 (2011).
15. M. Xu and R. R. Alfano, *Neurophotonics and Biomedical Spectroscopy*, pp. 521–545, Elsevier Ltd. (2018).
16. M. Guney, B. Tunc, and M. Gulsoy, "Investigating the ablation efficiency of a 1940-nm thulium fiber laser for intraoral surgery," *Int. J. Oral Maxillofac. Surg.* **43**(8), 1015–1021 (2014).
17. H. D. Downing and D. Williams, "Optical constants of water in the infrared," *J. Geophys. Res.* **80**(12), 1656–1661 (1975).
18. J. A. Harrington, "Introduction to infrared fiber optics," *Infrared Fibers and Their Applications*, pp. 1–9, SPIE Press, Bellingham, Washington (2004).
19. A. J. Welch and M. J. C. van Gemert, *Optical-Thermal Response of Laser-Irradiated Tissue*, pp. 44–45, Springer, Dordrecht (2011).
20. S. Amini-Nik et al., "Ultrafast mid-IR laser scalpel: protein signals of the fundamental limits to minimally invasive surgery," *PLoS One* **5**(9), e13053 (2010).
21. R. E. Friedrich et al., "Ablation precision and thermal effects of a picosecond infrared laser (PIRL) on roots of human teeth: a pilot study ex vivo," *In Vivo* **34**(5), 2325–2336 (2020).
22. R. L. Blackmon, P. B. Irby, and N. M. Fried, "Enhanced thulium fiber laser lithotripsy using micro-pulse train modulation," *J. Biomed. Opt.* **17**(2), 028002 (2012).
23. H. Z. Alagha and M. Gülsoy, "Photothermal ablation of liver tissue with 1940-nm thulium fiber laser: an ex vivo study on lamb liver," *J. Biomed. Opt.* **21**(1), 015007 (2016).

24. A. Vogel and V. Venugopalan, "Mechanisms of pulsed laser ablation of biological tissues," *Chem. Rev.* **103**(2), 577–644 (2003).
25. R. Phelan et al., "In0.75Ga0.25As/InP multiple quantum-well discrete-mode laser diode emitting at 2 μm," *IEEE Photonics Technol. Lett.* **24**(8), 652–654 (2012).
26. A. Kobyakov, M. Sauer, and D. Chowdhury, "Stimulated Brillouin scattering on optical fibers," *Adv. Opt. Photonics* **2**(1), 1–59 (2010).
27. G. L. Keaton et al., "Stimulated Brillouin scattering of pulses in optical fibers," *Opt. Express* **22**(11), 13351–13365 (2014).
28. A. Sincore et al., "SBS threshold dependence on pulse duration in a 2053 nm single-mode fiber amplifier," *J. Lightwave Technol.* **35**(18), 4000–4003 (2017).
29. R. Paschotta, "Gain-switching," RP Photonics, 2007, https://www.rp-photonics.com/gain_switching.html (accessed 21st May 2024).
30. R. Paschotta, "Spiking," RP Photonics, 2007, https://www.rp-photonics.com/spiking.html (accessed 21st May 2024).
31. J. Trägårdh et al., "A simple but precise method for quantitative measurement of the quality of the laser focus in a scanning optical microscope," *J. Microsc.* **259**(1), 66–73 (2015).
32. J. Schindelin et al., "Fiji: an open-source platform for biological-image analysis," *Nat. Methods* **9**(7), 676–682 (2012).
33. R. R. Anderson and J. A. Parrish, "Selective photothermolysis: precise microsurgery by selective absorption of pulsed radiation," *Science* **220**(4596), 524–527 (1983).
34. I. T. Young et al., "Depth-of-focus in microscopy," in *Proc. 8th Scand. Conf. Image Anal.*, pp. 493–498 (1993).
35. R. Cheng et al, "Influence of fixation and permeabilization on the mass density of single cells: a surface plasmon resonance imaging study," *Front. Chem.* **7**, 588 (2019).
36. T. Van Acker et al., "High-resolution imaging and single-cell analysis via laser ablation-inductively coupled plasma-mass spectrometry for the determination of membranous receptor expression levels in breast cancer cell lines using receptor-specific hybrid tracers," *Anal. Chim. Acta* **1074**, 43–53 (2019).
37. P. Zhao et al., "Femtosecond laser microdissection for isolation of regenerating C. elegans neurons for single-cell RNA sequencing," *Nat. Methods* **20**, 590–599 (2023).
38. F. Mangione et al., "Photoablation at single cell resolution and its application in the Drosophila epidermis and peripheral nervous system," *Front. Physiol.* **13**, 1093303 (2023).

Matthew D. Gerard received his MPhys degree from the University of St Andrews and subsequently joined the Optoelectronics Research Center, a constituent department of the University of Southampton, in 2021. His interests include the development of advanced thulium-doped pulsed fiber lasers for applications in the medical industry, particularly mechanisms of pulsed laser ablation. More recently, his research has focused on harnessing the mechanisms of pulsed laser ablation to optimize and broaden the scope of its application.

Hiroki Cook joined the Molecular Biophotonics and Imaging group at the University of Southampton, following the award of his MPhys degree in 2020. His research focuses on spectroscopic techniques in the near and shortwave infrared for label-free, non-destructive, deeply penetrating diagnostics and in developing photo-ablation processes for therapeutic application.

James A. Read is a research fellow at the University of Southampton in the School of Chemistry. He received his integrated MS degree in science in Forensic Science from Sheffield Hallam University and completed his PhD, in the field of coherent Raman imaging, at the University of Southampton. His current field of research is label-free and Raman imaging, light sheet microscopy, and super-resolution microscopy.

Ibrahim H. Abughazaleh is a PhD student at the Optoelectronics Research Centre (ORC), University of Southampton, United Kingdom. He received his master's degree in medical engineering from Cardiff University, United Kingdom. His current research topic covers advanced fiber laser technology for deep-tissue medical imaging in which mode-locked thulium-doped fiber laser techniques and adaptive pulse shaping methods are under development.

Panuwat Srisamran received his BS and MS degrees in physics from the Prince of Songkla University, Thailand. In 2021, he started his PhD at the Optoelectronics Research Centre (ORC), University of Southampton, United Kingdom. His research focuses on the design and study of high-power ultrashort-pulsed mode-locked thulium-doped fiber lasers for healthcare applications, particularly for deep-layer biomedical imaging.

Siddhi Chugh is a PhD student with the Molecular Biophotonics and Imaging Group at the University of Southampton, United Kingdom. Her research focuses on the study of temporal bone development and regeneration with the aid of organotypic cultures using label-free and non-invasive multimodal imaging in contrast to invasive methodologies, i.e., histological analysis or micro-computed tomography.

Sijing Liang received her PhD in optoelectronics from the Optoelectronics Research Centre (ORC) of the University of Southampton in 2019. She studied high-power short-pulse thulium-doped fiber lasers and their relevant applications during her PhD. She is currently a research fellow at the ORC, and her research interests include multicore fiber amplifiers and two-micron fiber lasers.

Qiang Fu received his PhD from the Optoelectronics Research Centre (ORC) at the University of Southampton, United Kingdom, in 2021, working on developing novel light sources in the mid-infrared region. He is currently a research fellow at the ORC where his work spans hollow-core fibers, high-power lasers, and their applications in industry and biomedicine. He also serves as a chair of the Optica technical group "Lasers in Manufacturing."

Richard O. C. Oreffo holds the chair of Musculoskeletal Science and is internationally recognized for his work on skeletal stem cells and bone regeneration. Richard has trained 56 MD/PhD interdisciplinary scientists, published widely (>370 papers) with breakthrough publications on skeletal stem cells, osteoarthritis, and bone regeneration, and holds nine patents. He is the founder/CSO of Renovos Biologics Limited, a fellow of the Royal Society of Biology, International Orthopaedic Research, and a fellow of the Academy of Medical Sciences.

David J. Richardson is a deputy director of the Optoelectronics Research Centre/Zepler Institute and is the head of the ORC fiber and laser Group. He has worked on a diverse array of optical fiber-related research topics during his >30-year career at the ORC including the development of novel forms of optical fiber, telecommunications, high-power fiber lasers, and distributed optical fiber sensors. He is globally recognized as a leading authority in optical fiber technology and its applications.

Sumeet Mahajan is a professor in Molecular Biophotonics jointly between the School of Chemistry and the Institute of Life Sciences at the University of Southampton. His research focuses on developing optical techniques and instrumentation to extract chemical information in a label-free manner from biological systems to understand disease processes for early, faster, or more sensitive diagnostics. Application areas include biofilm and anti-microbial resistance detection, and treatment and development of novel 3D imaging methods.

Lin Xu has expertise in ultrafast fiber lasers and nonlinear optics. He obtained his PhD in laser engineering from the Shanghai Institute of Optics and Fine Mechanics (SIOM), Chinese Academy of Science, China, in 2012. He has been working in the Optoelectronics Research Centre (ORC) at the University of Southampton, United Kingdom, since 2013. He is currently a principal research fellow at the ORC and leads research on mode-locked fiber lasers and nonlinear frequency conversions for applications including telecommunication, spectroscopy, and healthcare. He is a committee member of the Nonlinear Optics Technical Group of Optica.